Exhibit H

Original Article

First In-Human Magnetic Resonance Visualization of Surgical Mesh Implants for Inguinal Hernia Treatment

Nienke Lynn Hansen, MD,* Alexandra Barabasch, MD,* Martina Distelmaier, MD,*
Alexander Ciritsis, Dipl-Ing,* Nicolas Kuehnert, MD,† Jens Otto, MD,† Joachim Conze, MD,†
Uwe Klinge, MD,† Ralf-Dieter Hilgers, PhD,‡ Christiane K. Kuhl, MD,* and Nils Andreas Kraemer, MD*

Objectives: Until today, there have been no conventional imaging methods available to visualize surgical mesh implants and related complications. In a new approach, we incorporated iron particles into polymer-based implants and visualized them by magnetic resonance imaging (MRI).

After clinical approval of such implants, the purposes of this study were to evaluate the MRI conspicuity of such iron-loaded mesh implants in patients treated for inguinal hernias and to assess the immediate postsurgical mesh configuration.

Materials and Methods: Approved by the ethics committee, in this prospective cohort study, 13 patients (3 patients with bilateral hernia treatment) were surgically treated for inguinal hernia receiving iron-loaded mesh implants between March and October 2012. The implants were applied via laparoscopic technique (transabdominal preperitoneal technique; n = 8, 3 patients with bilateral hernia treatment) or via open surgical procedure (Lichtenstein surgery; n = 5). Magnetic resonance imaging was performed 1 day after the surgery at a 1.5-T scanner (Achieva; Philips, Best, The Netherlands) with a 16-channel receiver coil using 3 different gradient echo sequences (first gradient echo sequence, second gradient echo sequence, and third gradient echo sequence [GRE1-3]) and 1 T2-weighted turbo spin-echo sequence (T2wTSE). Three radiologists independently evaluated mesh conspicuity and diagnostic value with respect to different structures using a semiquantitative scoring system (1, insufficient; 2, sufficient; 3, good; 4, optimal). Mesh deformation and coverage of the hernia were visually assessed and rated using a 5-point semiquantitative scoring system. Statistical analysis was performed using mixed models and linear contrast.

Results: All 16 implants were successfully visualized by MRI. On gradient echo sequences, the mesh is clearly delineated as a thick hypointense line. On T2wTSE, the mesh was depicted as a faint hypointense line, which was difficult to identify. The first gradient echo sequence was rated best for visual conspicuity (mean [SD], 3.8 [0.4]). T2-weighted turbo spin-echo sequence was preferred for evaluation of the surrounding anatomy (mean [SD], 3.7 [0.3]). For the combined assessment of both mesh and anatomy, GRE3 was rated best (mean [SD], 2.9 [0.7]). Local air slightly reduced mesh delineation (lowest mean [SD] rating, 2.9 [0.7] for GRE3). Overall, in both implantation techniques, the meshes exhibited mild to moderate deformations (mean [SD], 3.3 [0.4], 3.1 [0.3], and 2.8 [0.3] on average with open technique, 2.7 [0.3], 2.7 [0.2], and 2.3 [0.3] with laparoscopic technique). Coverage of the hernia was achieved in 15 of the 16 implants.

Conclusions: Combining iron-loaded implants and MRI, we achieved mesh visualization for the first time in patients. For MRI protocol, we propose a combination of different gradient echo sequences and T2-weighted turbo spin-echo sequences: first gradient echo sequence for mesh configuration, T2wTSE for anatomy assessment, and GRE3 for evaluation of hernia coverage and mesh localization. Using our approach, MRI could become a noninvasive alternative to open surgical exploration if mesh-related complications were suspected.

Key Words: magnetic resonance imaging, iron-loaded textile mesh implants, inguinal hernia

(*Invest Radiol* 2013;48: 770–778)

The lifetime risk for developing an inguinal hernia is 27% for men and 3% for women.[1] Its repair is one of the most frequently performed operations in general surgery worldwide.[2] In recent years, the use of surgical implants to seal hernias has increased because of a lower rate of hernia recurrences, ease of use, and low morbidity rates.[3]

The most common clinically used implants consist of either polymer meshes or sheets.[4] Via different techniques, either open surgery or minimal access laparoscopy, the mesh implant is inserted either anteriorly via the groin or posteriorly via the preperitoneal plane.[5] After implantation between the layers of the abdominal wall, the mesh is incorporated by fibrous tissue. The amount of tissue reaction depends on the inserted material and its pore size.[6]

Scar tissue formation can lead to contraction, shrinkage, and deformation of mesh implants. This implant deformation is commonly blamed for severe mesh related complications such as migration and penetration into abdominal organs, fistula formation, and, most of all, chronic pain, which can occur in up to 30% of cases.[7–11]

Surgical mesh implants are commonly made of alloplastic polymers and cannot be depicted using conventional radiological methods. Although previous studies have evaluated regular mesh implants ex vivo and in vivo using magnetic resonance imaging (MRI),[12–15] the depiction of the implant and its delineation with respect to adjacent anatomic structures remains challenging. Consequently, patients with suspected mesh related problems often undergo a surgical exploration. The thin polymer threads (<150 μm), the mesh implant's base material, do not yield a detectable magnetic resonance (MR) signal because of very short T2 relaxation times.[16,17] Recently, an approach to visualize surgical textile implants using MRI has been established.[18–20] Tiny iron particles integrated into the mesh base material induce local susceptibility differences, which can be depicted as signal voids.[18] In previous animal examinations, this approach was demonstrated in vivo.[21,22] In these studies, the mesh implants were located in the abdominal wall of small animals; moreover, the meshes were positioned in a very plain configuration. After clinical approval of this mesh technology, this study was initiated to investigate textile implants in an anatomically complex, clinical setting in patients. The purposes of the study were to establish an MRI sequence protocol by evaluating different MR sequences and to assess the immediate postsurgical findings.

MATERIALS AND METHODS

Study Population

This prospective cohort study was approved by the local ethics committee (code no. 194/11), and all patients provided written in formed consent. Between March and September 2012, a total of 13 patients (12 men, 1 woman; age range, 37 77 years; median age, 64 years) with symptomatic inguinal hernias were recruited by the De partment of Abdominal Surgery. All surgical procedures were performed by abdominal surgeons with more than 6 years of expe rience in open and laparoscopic hernia repair. Eight of the patients received the mesh via laparoscopic (transabdominal preperitoneal technique [TAPP]) technique. Five patients received the mesh via open (Lichtenstein) technique. Three patients received bilateral her nia repair, all of them via laparoscopic approach.

Surgical Mesh Implants

All surgical mesh implants used either for TAPP or for Lich tenstein surgery consisted of polyvinylidenfluoride monofilaments. To provide MR visibility, tiny iron particles have been embedded into the base material, resulting in a mesh concentration of 99% polyvinylidenfluoride and 1% Fe_3O_4. The meshes were assembled by FEG Textiltechnik mbH (DynaMesh Lichtenstein visible [PV170715] with 50% MR visible filaments/DynaMesh Endolap visible [PV141015] with 25% MR visible filaments; FEG Textiltechnik mbH, Aachen, Germany) with a size of 10×15 cm (Fig. 1). The meshes were assembled to fit the respective surgical procedure; the DynaMesh Lichtenstein therefore contains 2 tailed parts, whereas the DynaMesh Endolap consists of a continuous mesh.
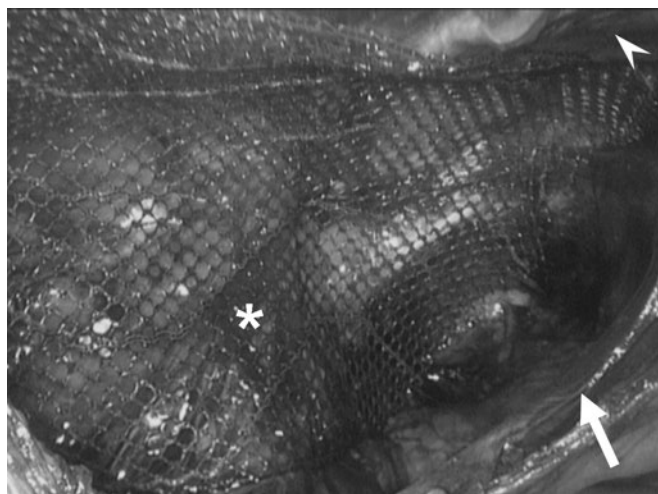
Surgical Procedures

Transabdominal Preperitoneal Technique

Via standard laparoscopic technique, the peritoneal space is accessed and expanded by carbon dioxide insufflations. After blunt dissection of the peritoneum and the abdominal wall, the hernial sac is resected. The mesh implant, which can optionally be trimmed to
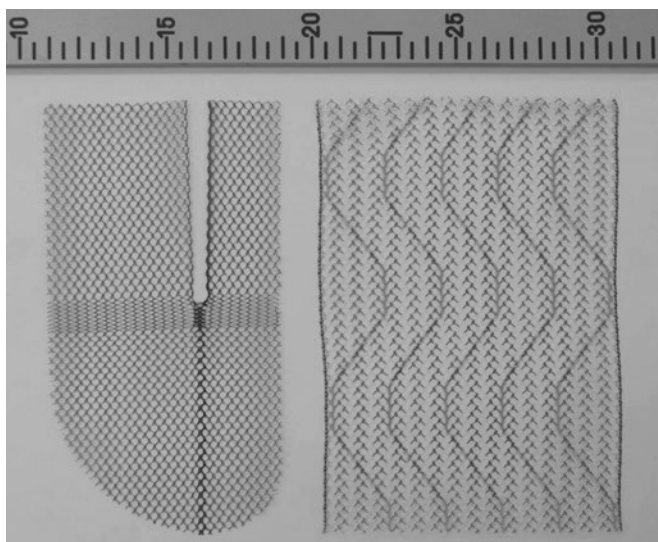
FIGURE 2. Laparoscopic view of a patient's groin during the TAPP procedure. The mesh implant (asterisk) is placed in the preperitoneal space between the anterior abdominal wall (arrowhead) and the peritoneum (arrow).
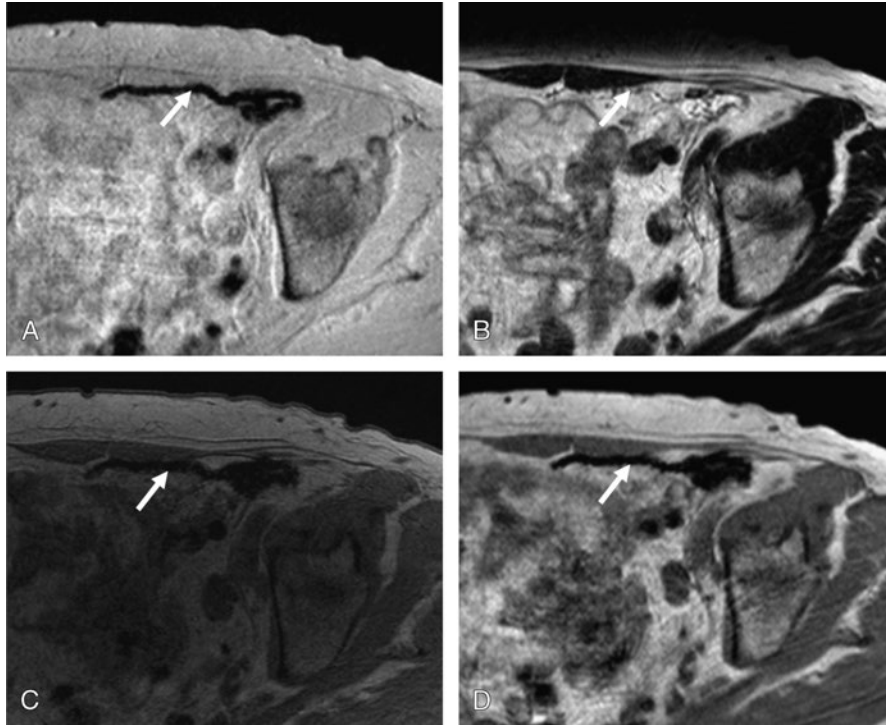
fit, is then placed in the preperitoneal space posteriorly to the ab dominal wall (posterior approach). There, it covers the internal ring, the testicular vessels, and the spermatic cord laterally; the Hesselbach triangle medially; and the Cooper ligament inferiorly[23] (Fig. 2). The implant is fixed in its correct position by glue application.

Lichtenstein Technique

In open Lichtenstein technique, the inguinal canal is opened transcutaneously and the hernial sac is resected. A sheet of prosthetic mesh is placed on the canal floor anteriorly to the abdominal wall (anterior approach), covering the pubic tubercle, the Hesselbach tri angle, and the internal ring. Two laterally positioned tails of the mesh are then crossed behind the spermatic cord. The mesh is secured by continuous sutures.[24,25]

Magnetic Resonance Imaging

On day 1 or 2 after the surgery, all patients underwent MR examinations on a clinical 1.5 T scanner (Achieva; Philips, Best, The Netherlands). A multichannel receiver coil was used to acquire the signal (Sense XL Torso Coil; Philips Healthcare, The Netherlands). The MR sequence protocol included 3 conventional gradient echo and 1 T2 weighted turbo spin echo sequences in transverse orienta tion. One gradient echo sequence is a radio frequency (RF) spoiled multishot gradient echo sequence (GRE1) that has been used in previ ous animal studies and that has been selected because of pronounced susceptibility artifacts and a relatively hyperintense surrounding. The other 3 sequences are slightly adapted versions of our clinically used sequences. The T2 weighted turbo spin echo sequence (T2wTSE) is part of the routine protocol for pelvic MRI. The second gradient echo sequence is a modified version of a robust T1 weighted non RF spoiled gradient echo sequence (GRE2) that is routinely used for abdominal and liver MRI. The third gradient echo sequence is an adaption of a T1 weighted non RF spoiled gradient echo se quence (GRE3) that is used as a precontrast/postcontrast dynamic in gynecological MRI examinations. This sequence was chosen to compare the influence of bandwidth variation. Sequence param eters of these sequences were as follows: (1) GRE1: repetition time (TR), 8.3 milliseconds; echo time (TE), 4.6 milliseconds; number of signal acquisitions (NSA), 2; flip angle (FA), 20 degrees;

FIGURE 1. Photograph of the 2 types of mesh implants used. Left, DynaMesh-Lichtenstein visible (FEG Textiltechnik mbH, Aachen, Germany) for open hernia treatment (the Lichtenstein procedure). Right, DynaMesh-Endolap visible (right; FEG Textiltechnik mbH, Aachen, Germany) for laparoscopic hernia treatment (the TAPP procedure).

FIGURE 3. Transversely orientated MR images of a patient's groin after the laparoscopic mesh implantation. The mesh implant (arrows) is located on the left. A, In GRE1, the mesh-induced signal voids (arrow) clearly contrast to the surrounding hyperintense anatomy, resulting in precise delineation. B, T2-weighted turbo spin-echo sequence presents the anatomy clearly, whereas the implant is shown only as a faint dotted line (arrow) that is difficult to distinguish from other hypointense structures. C and D, GRE2 (C) and GRE3 (D) were preferred by the readers for a combined assessment of both the surrounding anatomy and the mesh (arrows), with a slight preference for GRE3.

bandwidth, 215 hertz per pixel; field of view (FOV), 350 mm^2; voxel size, 0.95×0.97 mm^2; slice thickness, 5 mm; and scan duration, 2 minutes 26 seconds; (2) GRE2: TR, 362 milliseconds; TE, 4.7 milliseconds; NSA, 1; FA, 90 degrees; bandwidth, 167 hertz per pixel; FOV, 350 mm^2; voxel size, 0.6×0.74 mm^2; slice thickness, 5 mm; and scan duration, 2 minutes 9 seconds; (3) GRE3: TR, 244 milliseconds; TE, 4.6 milliseconds; NSA, 3; FA, 80 degrees; bandwidth, 567 hertz per pixel; FOV, 350 mm^2; voxel size, 0.9×1.1 mm^2; slice thickness, 5 mm; and scan duration, 1 minute 59 seconds; and (4) conventional turbo spin echo sequence (T2wTSE): TR, 4372 milliseconds; TE, 80 milliseconds; NSA, 3; FA, 90 degrees; FOV, 360 mm^2; voxel size, 0.7×1.04 mm^2; slice thickness, 4 mm; and scan duration, 3 minutes 30 seconds. The first 4 patients (one with bilateral mesh treatment) were examined only with GRE1 and T2wTSE. In the remaining 9 patients (3 with bilateral mesh treatment), the sequence protocol was extended by GRE2 and GRE3.

Image Analysis

Three radiologists (blinded for review) reviewed the obtained images independently. The readers were asked to score the respective pulse sequences with respect to conspicuity and diagnostic value. To assess conspicuity, 5 criteria were established: (1) Visual contrast to noise ratio of the mesh to score the confidence with which radiologists were able to identify at all the mesh implant on the images, (2) conspicuity to local air artifacts to describe the radiologists' ability to identify the mesh implant on the basis of specific susceptibility effects and to differentiate them from other signal voids, and (3) diagnostic quality rating with respect to (*a*) the mesh to communicate the radiologist's confidence to establish a diagnosis of mesh structure, (*b*) the surrounding anatomic structures for diagnosis of mesh

related complications, and (*c*) the mesh in relation to the hernia for diagnosis of possible mesh migration. The following 4 point grading scale was used for these conspicuity criteria: 1, insufficient; 2, sufficient; 3, good; and 4, optimal. For evaluating their diagnostic value, the pulse sequences were scored using the following 2 criteria: (*a*) amount of mesh deformation and (*b*) localization of the mesh in relation to the hernia and/or the inguinal canal. A 5 point grading scale was used for these 2 criteria: (*a*) for mesh deformation: 0, not applicable; 1, no deformation; 2, mild deformation; 3, moderate deformation; and 4, severe deformation with loss of basic configuration; and (*b*) for localization: 0, not applicable; 1, hernia not covered; 2, hernia partially covered; 3, hernia entirely covered but merely with the periphery of the mesh; and 4, hernia entirely covered with the center of mesh.

For additional diagnostic evaluation, general radiological appearance of the mesh and the anatomy such as gross mesh structure, local folds, or contact to organs and vessels was assessed and findings were reported.

Statistical Analysis

The mean rating and SD for each criterion and sequence were calculated. For statistical significance, a mixed linear model was fitted to the data with random intercept, repeated grouping factor (reader × criterion × sequence), and fixed effects (surgical procedure, sequence, criterion, reader, side of surgery, and quality by sequence interaction). This resulted in separate statistical models: one for visual contrast to noise ratio (vCNR) and local air artifacts, another for mesh and anatomy rating, respectively, and a third one for mesh and anatomy in a combined criterion. In case of significant effects, linear contrasts were used for further analysis. Significance levels were set to
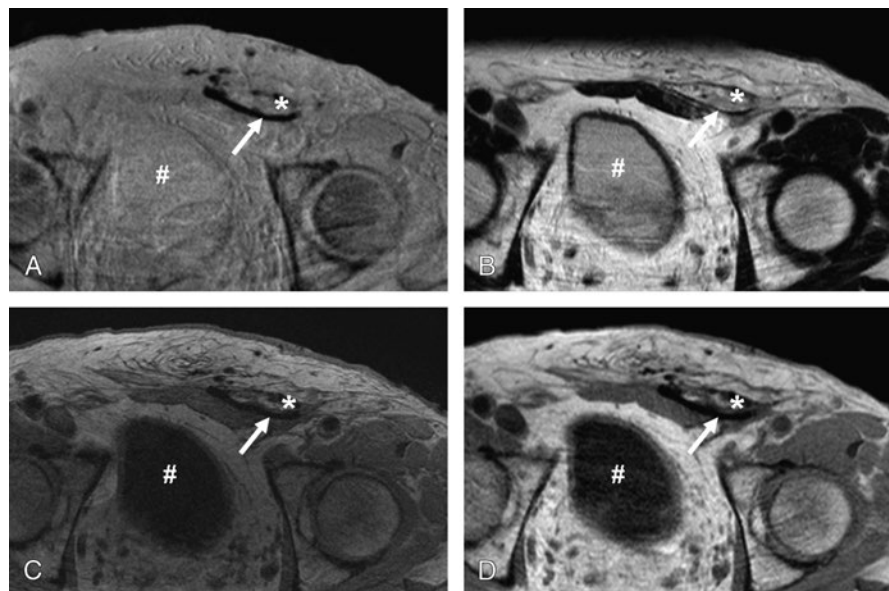
FIGURE 4. Axial view of a patient's groin after the open mesh implantation (Lichtenstein) on the left. The arrows show the mesh implant; the asterisk symbol (*) indicates the inguinal canal and the hash (#) marks the bladder using the following sequences: GRE1 (A), T2wTSE (B), GRE2 (C), and GRE3 (D).

5%. SAS (version 9.2, TS2M3, 64 Bit for Windows 7; SAS Institute Inc, Cary, NC) statistical software (Proc MIXED) was used for computations.

RESULTS

Mesh Conspicuity

In all 13 patients, the mesh implants (n 16; 3 patients with bilateral hernia treatment) were successfully visualized by MRI. Generally, gradient echo sequences depicted the implants and distinguishable susceptibility induced signal voids (Figs. 3A D and Figs. 4A D), whereas T2wTSE exhibited merely faint and difficult to distinguish signal voids. Visually, no differences of the mesh artifacts were seen between the 2 mesh designs used for the respective surgical technique (TAPP or Lichtenstein). With respect to image impairment through local air voids, the readers were able to differentiate the mesh well from local air in all GRE and T2wTSE sequences because signal voids from mesh induced susceptibility artifacts were generally smaller and presented a more regular pattern compared with various, often irregular aspects of air collections. Moreover, the susceptibility artifacts had more blurred edges compared with the sharper rim of air pockets. The resulting image quality was rated between 2.9 (SD, 0.7) and 3.5 (SD, 0.5) in all cases. The detailed mean scores for all sequence ratings are given in Table 1. Table 2 lists the results of the 3 different mixed models used for the statistical analysis in detail. The influence analysis during model fitting of the mixed linear models required that patients 5 and 8 be excluded from the analysis in the first model; patient 5, only in the second model; and patient 8, only in the third model. As also shown in Table 1, the secondary analysis based on linear contrast revealed the following order of sequences according to statistical significance and mean rating (the greater than symbol (>) indicates higher mean and significant difference; the approximately equal to symbol (@) refers to similar mean scores with no statistically significant difference): visual contrast to noise ratio: GRE1 > GRE3 @ GRE2 > T2wTSE (P 0.0309, P 0.6337, $P < 0.0001$); conspicuity to local air artifacts: GRE1 > GRE2 @ T2wTSE @ GRE3 (P 0.0097, P 0.4157, P 0.0903); diagnostic quality of the mesh: GRE1 > GRE3 @ GRE2 > T2wTSE (P 0.0191, P 0.1200, $P < 0.0001$); diagnostic quality of the anatomy: T2wTSE > GRE2 > GRE3 > GRE1 ($P < 0.0001$, P 0.0139, P 0.0020); diagnostic

TABLE 1. Overview of the Mean Ratings the Individual Sequences Received for Each of the Conspicuity Criteria in the Image Analysis

Patients, N = 13 Sequence	vCNR Mean (SD) Rating	Conspicuity to Local Air Artifacts Mean (SD) Rating	Diagnostic Quality Rating (Mesh) Mean (SD) Rating	Diagnostic Quality Rating (Anatomy) Mean (SD) Rating	Diagnostic Quality Rating (Mesh + Anatomy) Mean (SD) Rating
GRE1 (a)	3.8 [b, c, d] (0.4)	3.5 [b, c] (0.5)	3.5 [b, c, d] (0.5)	2.2 [c, d] (0.9)	2.4 [b, c, d] (0.7)
GRE2 (b)	3.1 [a, d] (0.6)	3.0 [a] (0.7)	2.8 [a, d] (0.4)	2.9 [c, d] (0.4)	2.6 [a, c, d] (0.6)
GRE3 (c)	3.3 [a, d] (0.6)	2.9 [a] (0.7)	2.9 [a, d] (0.7)	2.8 [a, b, d] (0.3)	2.9 [a, b, d] (0.6)
T2wTSE (d)	1.9 [a, b, c] (0.6)	3.2 (0.8)	2.0 [a, b, c] (0.4)	3.7 [a, b, c] (0.3)	2.3 [a, b, c] (0.4)

The SD is given next to each value.
The indices a to d indicate significant differences to the referring sequences a, b, c, or d.
P values are given in the text.
GRE1 indicates first gradient echo sequence; GRE2, second gradient echo sequence; GRE3, third gradient echo sequence; T2wTSE, T2-weighted turbo spin-echo sequence; vCNR, visual contrast-to-noise ratio.

TABLE 2. Results of the Mixed Linear Model Calculations

Effect	Num DF	First Model: vCNR and Local Air Artifacts, Respectively			Second Model: Diagnostic Quality of the Mesh and of the Anatomy, Respectively			Third Model: Diagnostic Quality of the Mesh and the Anatomy Combined		
		Den DF	F Value	Pr > F	Den DF	F Value	Pr > F	Den DF	F Value	Pr > F
Procedure	1	207	15.32	0.0001	254	3.51	0.0621	120	5.71	0.0184
Sequence	3	207	44.78	<0.0001	254	3.60	0.0142	120	20.94	<0.0001
Side (right/left)	1	207	1.31	0.2531	254	1.09	0.2984	120	0.32	0.5726
Criteria	1	207	3.52	0.0619	254	0.00	0.9695			
Reader	2	207	4.25	0.0156	254	32.40	<0.0001	120	26.59	<0.0001
Sequence*criteria	3	207	35.15	<0.0001	254	110.41	<0.0001			

Num DF indicates numerator degrees of freedom; Den DF, denominator degress of freedom; F, Fisher statistic associated with the given effect; Pr > F, P value associated with the F statistic of the given effect; vCNR, visual contrast-to-noise ratio.

quality of the mesh and the anatomy combined: GRE3 > GRE2 > GRE1 > T2wTSE (P 0.0025, P 0.0172, P 0.0266). In the succeeding paragraphs, the appearance of the individual sequences is described.

First Gradient Echo Sequence

On GRE1 (all patients and meshes), the mesh clearly presented as a distinct line of signal voids with slight periodic ir regularities reflecting the mesh structure (Figs. 3A and 4A). All surrounding soft tissue structures exhibited almost homogenously hyperintense signals, merely distinguishable by faint hypointense outlines. This resulted in significantly highest (SD) visual contrast to noise ratio of all sequences (3.8 [0.4]) allowing for a detailed distinction between the mesh filaments and the hyperintense adjacent structures and a precise depiction of mesh folding and wrinkles in detail. The diagnostic quality regarding the mesh structure was rated highest (3.5 [SD, 0.5]) in GRE1 but was significantly lower regarding the diagnostic quality of the anatomy (2.2 [SD, 0.9]) compared with GRE2, GRE3, and T2wTSE.

T2-Weighted Turbo Spin-Echo Sequence

On T2wTSE, the mesh implant presented as a faint dotted line of small signal voids that was difficult to distinguish from the sur rounding soft tissue structures such as the hypointense muscles, the fascia, or the bowel, or from inhomogeneities in the fat tissue (Figs. 3B and 4B). Muscle tissue exhibited hypointense signals contrasting well with the intestinal fat and the fibrous tissue, allowing differentiation of the separate muscle layers. For the diagnostic quality regarding the anatomy, this sequence received the signif icantly highest rating (3.7 [SD, 0.3]). In all other criteria (vCNR, the diagnostic quality regarding the mesh, and the diagnostic quality of both mesh and anatomy), T2wTSE received the significantly lowest ratings (1.9 [SD, 0.6], 2.0 [SD, 0.4], and 2.3 [SD, 0.4], respectively; P < 0.03 for all combinations).

Second Gradient Echo Sequence

In GRE2 (n 9 patients, n 11 mesh implants), the mesh presented less detailed than that in GRE1 as a blurred line of signal voids (Figs. 3C and 4C). Mesh configuration changes were depicted as larger signal voids that did not allow for a detailed assessment of folding. Generally, the contrasts between the tissues were visually high, especially between the hypointense muscles and the hyperintense fat. Compared with GRE1 (2.4 [SD, 0.7]), this resulted in a similar rating regarding the anatomy (2.9 [SD, 0.6]; P 0.0835). However, the mean (SD) rating score for vCNR under GRE2 was 3.1 (0.6) and was thus significantly lower than the mean (SD) score of that under GRE1 (3.8 [0.4]; P 0.0020). For the diagnostic quality

rating regarding the mesh structure, the mean (SD) ratings are as follows: GRE2 (2.8 [0.4]) versus GRE1 (3.5 [0.5]); P < 0.0001). Regarding the overall diagnostic quality combining the mesh and anatomy assessment, GRE2 was rated significantly superior (2.6 [SD, 0.6]) to GRE1 (2.4 [SD, 0.7]; P 0.0172) and significantly inferior to GRE3 (2.9 [SD, 0.6]; P 0.0025).

Third Gradient Echo Sequence

In GRE3 (n 9 patients, n 11 mesh implants), the mesh presented as a slightly blurred line of signal voids visually less dis tinct than the ones in GRE1 but more distinct compared with that in GRE2 (Figs. 3D and 4D). Visually, the muscles and the bowel presented with less signal compared with those in GRE1. Compared with GRE2, GRE3 visually exhibited slightly more tissue contrast. vCNR between the mesh and the adjacent structures was rated with 3.3 (SD, 0.6), which was worse than GRE1 (3.8 [SD, 0.4]; P 0.0309) but similar to GRE2 (3.1 [SD, 0.6]; P 0.6337). Mesh configuration changes were depicted as large signal voids instead of detailed folding, visually similar to GRE2. The diagnostic quality rating regarding the mesh structure was worse than GRE1 (2.9 [SD, 0.7] vs 3.5 [SD, 0.5]; P 0.0191). Regarding the overall diagnostic quality combining the mesh and anatomy assessment, GRE3 (2.9 [SD, 0.6]) scored slightly higher than GRE2 (2.6 [SD, 0.6]; P 0.0025).

Mesh Configuration and Localization

Most mesh implants (15 of 16) in both laparoscopic and open implantation exhibited mild to moderate deformation. See Figures 5A to D for image examples of the different categories of mesh de formation. None of the mesh implants presented without any defor mation. Seven of the 16 mesh implants presented with little deformation (44%); 8 of the 16, with moderate deformation (50%). One implant (6%) showed severe deformation. No difference in configuration was found between open and laparoscopic implanta tion techniques.

Radiological Appearance

Transabdominal Preperitoneal Technique Implants (n = 11)

When placed via laparoscopic approach, the implants usually stretched several centimeters along the inner abdominal wall down to the symphysis (Figs. 3 and 6). The medial parts of the meshes formed more or less pronounced wavelike configurational changes. In some cases, these parts of the meshes were in close contact to the bowel (10 of 11); in the more caudal parts, adjacent to the urinary bladder (9 of 11). In the pelvis, the mesh implant extended along the superior branch of the pubic bone to the corner of the peritoneal cavity where the inner ring of the inguinal canal is located. There, the lateral part
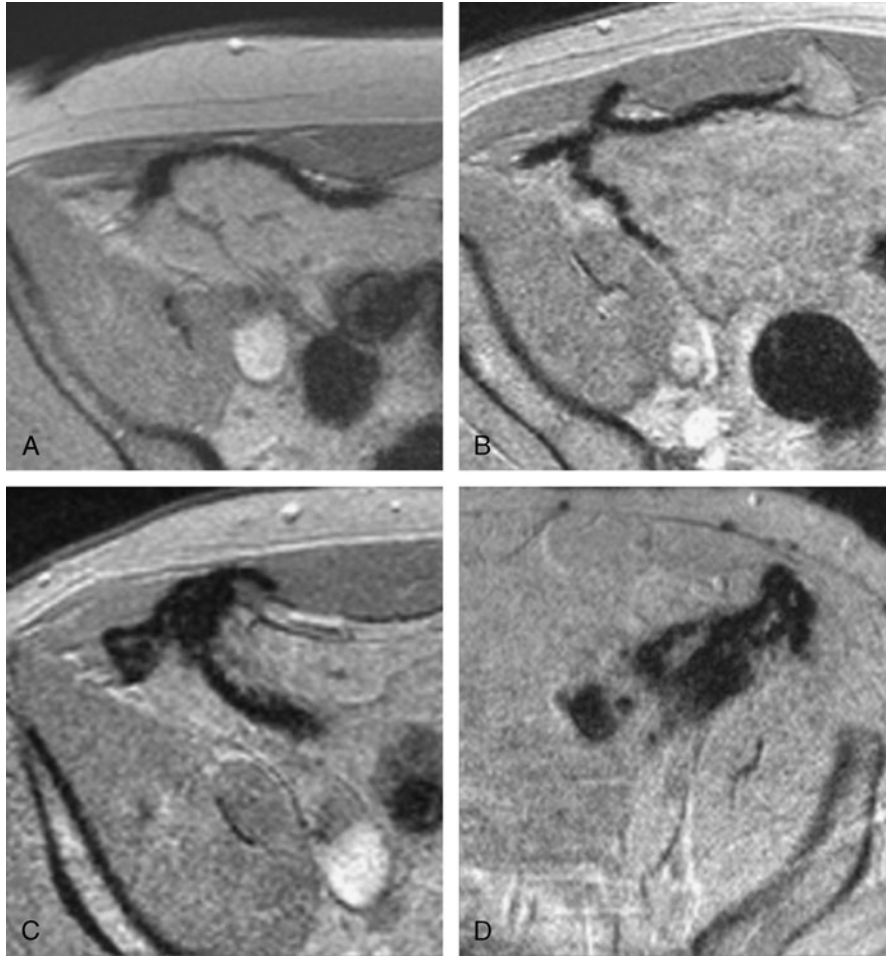
FIGURE 5. Different examples of postsurgical mesh deformation in the patient's groins on GRE1. Mesh configuration was scored from 1 to 4 as follows: 1, no deformation (A); 2, mild deformation (B); 3, moderate deformation (C); and 4, severe deformation with complete loss of mesh configuration (D). On average, mesh deformation was rated as mild to moderate (2.2, on average, with the open Lichtenstein technique; 2.7, with the laparoscopic TAPP technique).

of the implant formed a T shaped or more complex accumulation of mesh folds, which was diagnosed in all TAPP implants. After this directional change toward the psoas muscle, the external iliac vessels provoked a distinct impression in the meshes (8 of 11). In general, folding was more pronounced along the edges of the TAPP mesh implants.

Lichtenstein Implants (n = 5)

With the Lichtenstein procedure, most mesh implants stretched anteriorly to the external border of the rectus abdominis muscle and the external oblique muscle, forming more or less pro nounced wavelike configuration changes, enforcing the posterior wall of the inguinal canal and covering the area most prone to medial hernia occurrence (Fig. 4A D). Because of the placing of the mesh anterior to the muscular wall, approximation of implants with bowel or intra abdominal organs did not occur.

Hernia Coverage

In 12 of the 13 patients (15 of the 16 meshes), coverage of the hernia was achieved as described previously (3.5, on average, with the laparoscopic technique; 3.6, with the open technique). Most of the implants covered the hernia entirely, either with the center of the

mesh (10/16, 63%) or with a peripheral area of the mesh (5/16, 31%). In 1 of the 16 implants (6%), the hernia was not covered at all.

DISCUSSION

To our knowledge, this study is the first to achieve complete visualization of mesh implants in patients using MRI. The integrated iron particles generated sufficient susceptibility differences to dis criminate the mesh implant versus its surrounding anatomy using gradient echo sequences. This facilitates a detailed assessment of mesh localization and configuration that is of therapeutic importance. In clinical practice, implant related complaints frequently occur after mesh based hernia treatment. To date, the only "diagnostic" ap proach has been the direct verification of mesh position and con figuration in a surgical exploration; moreover, a postsurgical assessment of mesh implants has not been possible under normal, noncomplicated conditions. Combining iron loaded meshes with MRI now gives the possibility to delineate the mesh implant in detail. This might help to improve hernia treatment in 2 ways. On the one hand, potential mesh related complications can be assessed accu rately and adequate treatment can be initiated. On the other hand, surgeons can learn about regular postsurgical mesh behavior and characteristics. Particularly, for surgeons learning this technique, the
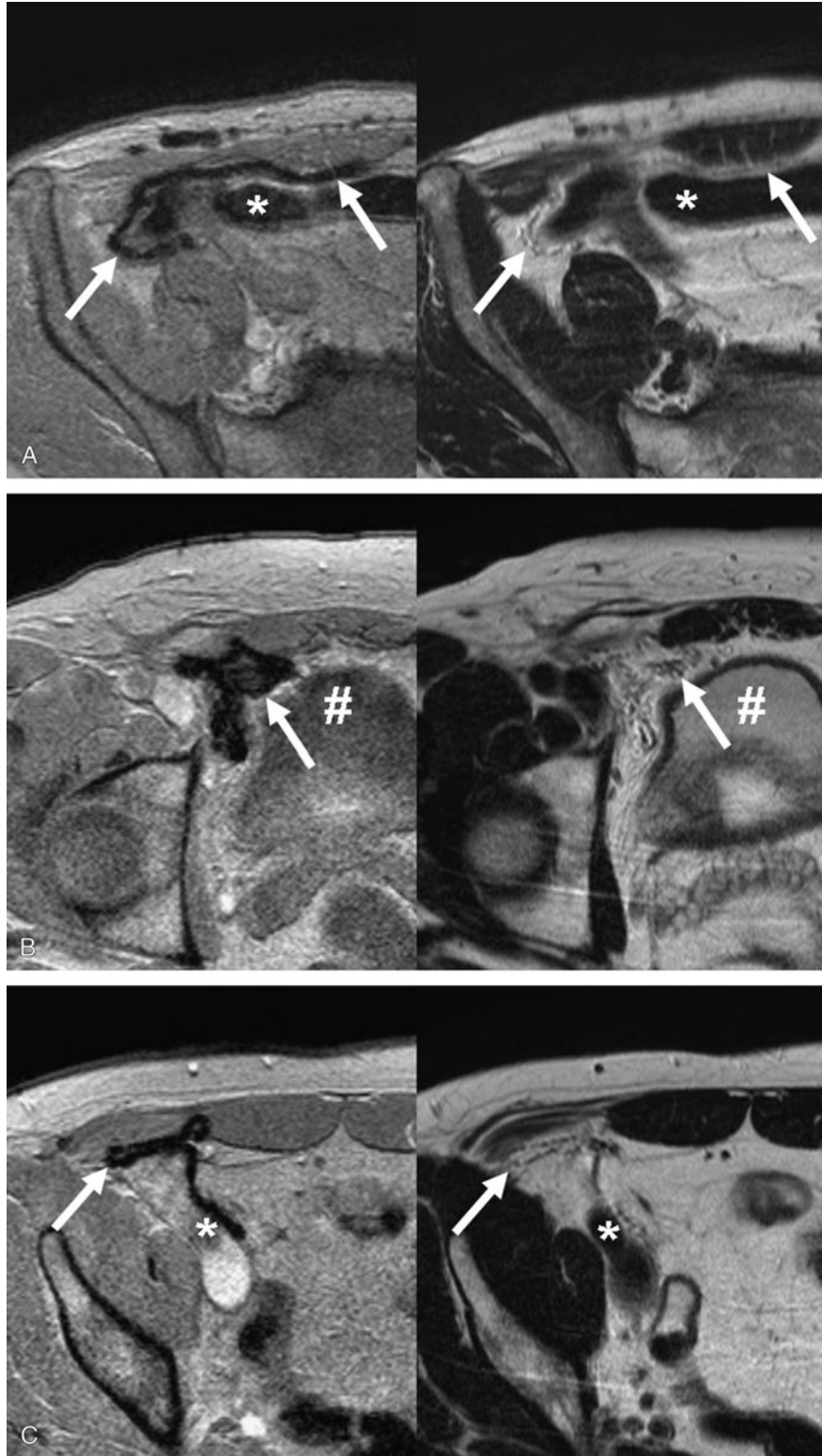
FIGURE 6. When placed via the laparoscopic approach (TAPP), the mesh implants exhibited characteristic configurational features as illustrated by the following examples on GRE1 and T2wTSE: A, The medial parts of the mesh (arrow) were in close contact to the bowel (asterisk), found with 10 of the 11 TAPP implants. B, The caudal parts of the mesh (arrow) were adjacent to the urinary bladder (#) in 9 of the 11 TAPP implants. C, The lateral part of the mesh (arrow) formed a T-shaped or more complex accumulation of mesh folds (arrow) in all TAPP implants. In 8 of the 11 implants, the external iliac vessels (*) provoked a distinct impression in the meshes that becomes more obvious when looking at a stack of images.

In-Human MR Visualization of Mesh Implants

close postoperative feedback of a correct mesh placement will help to improve their skills. Furthermore, for developers, this mesh visualization will help to design patient adapted implants.

In this study, the tested gradient echo sequences facilitated mesh delineation in all cases, although not in the same way. First gradient echo sequence exhibited the surrounding anatomy quite homogenously and hyperintensely, resulting in an excellent visual contrast to the distinct susceptibility artifacts of the iron loaded implant. Thus, the readers preferred this sequence to delineate the mesh and to assess its configuration. However, for the diagnostic evaluation of both, the sequence needs to exhibit the implant's susceptibility artifacts and the surrounding anatomy. The demand for these 2 criteria combined was met best by GRE3, followed by GRE2, although both sequences achieved lower ratings in the individual categories. Thus, these sequences were preferred by the readers to establish a diagnosis and to evaluate the mesh location referring to the hernia estimating the surgical success. However, these 2 sequences achieved lower ratings for explicit assessment of mesh configuration because the mesh implant presented as thicker and more blurred compared with GRE1.

Using T2wTSE, the integrated iron particles do not influence T1 and T2[19]; only marginal susceptibility artifacts occur on sequences with refocusing pulses such as spin echo sequences. Similar to a previous study in animals,[21,22] the iron loaded polymer implants in this study predominantly presented via partial volume effects. Therefore, if not surrounded by hyperintense fat tissue but adjacent to hypointense structures, a clear delineation of the mesh is challenging. Moreover, in cases of mesh folding, the faint dotted line in T2wTSE can no longer be discriminated continuously but appears as a dotted cluster that hampers a precise delineation of mesh continuity. Consequently, T2wTSE was rated worst for mesh delineation. However, for exclusive depiction of the surrounding anatomy, T2wTSE sequences achieved excellent reader's ratings. This can be attributed to distinct contrasts, a sharp image impression facilitating a fine delineation between the different structures and an image impression well known from diagnostic MRI of the pelvis.

In a previous study, positive contrast imaging was proposed to discriminate the susceptibility artifacts of the mesh from intestinal or postsurgical air.[22] Such techniques imply relatively long signal acquisition timing and are very susceptible to moving artifacts. As in this study, we used free breathing and we did not establish such positive contrast sequences. Nevertheless, on any sequence used in this study, the signal voids from the implant could clearly be discriminated against intestinal or postsurgical air because of their different appearance.

For precise radiological assessment, GRE1 and T2wTSE specifically focused on detailed information regarding mesh delineation or anatomic assessment, respectively. The third gradient echo sequence was preferred for overall mesh assessment in relation to the anatomy. Thus, as an MR pulse sequence protocol, both GRE1 and T2wTSE as well as GRE3 should be applied for detailed mesh evaluation.

Using the presented approach of iron particles incorporation into the mesh base material now not only allows MR visualization and discrimination of the mesh implants but also facilitates an assessment of configuration and localization. In this study, both laparoscopically (the posterior approach by TAPP) and openly (the anterior approach by Lichtenstein) implanted meshes exhibited mild to moderate postoperative deformation in the immediate postsurgical situation without statistical differences between both procedures. With the Lichtenstein technique, these deformations are not surprising because, in the procedure, the implant is folded within the curve of the inguinal canal and the tails are crossed. In TAPP, however, the implant is placed and fixed rather smoothly against the abdominal wall. One simple explanation for the postsurgical deformations could

be the deflation of the peritoneal cavity. However, it is also possible that the meshes are more mobile with this approach compared with the open technique and therefore exhibit postoperative dislocation within the preperitoneal space.

Using our technique, we were able to determine the exact localization of the mesh implant in relation to the adjacent anatomic structures. Coverage of the hernia was also achieved without statistical differences between both procedures. However, compared with the openly implanted meshes, the laparoscopically implanted meshes exhibited 4 unique characteristics: (1) contact to the anterior bladder wall with the caudal part of the mesh, (2) close position to the bowel with the medial part of the mesh, (3) accumulation of folds in the lateral part of the mesh, and (4) distinct iliac vessel impression. These characteristics are merely an observation at the time of the MRI examination in prone position because our analysis was focused on the immediate postsurgical conspicuity of the mesh. It would consequently be interesting to evaluate whether mesh configuration or localization of the meshes changes intraindividually both because of patient movement and, in the course of time, because of scar formation. Furthermore, it has to be examined whether such changes correlate with an increased occurrence of mesh migration, adhesion formation, and long term complications such as chronic pain or hernia recurrence. The use of iron loaded meshes now offers a feasible approach to answer these clinically important questions. The possibility to review the correct placement of mesh implants by MRI should consequently prevent unnecessary revision surgeries.

Our study has limitations such as the small number of patients included. However, because the mesh was successfully visualized in all 13 patients with the previously mentioned sequences, we are convinced that our results are clinically useful and suitable to establish a sequence protocol. The differences in mesh designs were not assessed separately because of equal appearance on visual assessment. In this study, we did not have surgical validation that configuration and localization of the mesh as depicted on MRI are actually correct; earlier studies using iron loaded mesh implants in small animals have shown that the images and the surgical position correlate.[22] Because, in our study, the mesh was so clearly delineated, we are confident that our image interpretation is realistic.

In conclusion, we have demonstrated, for the first time, that iron loaded implants can be visualized in patients using MRI and that it is possible to assess mesh deformation in detail. We therefore established a suggestion for an MR pulse sequence protocol, combining gradient echo and turbo spin echo sequences, to examine mesh delineation, assessment of the surrounding anatomy, and the relation of implant and the adjacent structures. This initial study shows that a considerable change in mesh configuration already occurs immediately after surgery. In the future, this combination of iron loaded textile implants and MRI might help to address important issues in mesh based hernia treatment, such as deformation, shrinkage, migration, or adhesions; most importantly, it might help patients and surgeons to examine potentially mesh related complaints, to evaluate the need for revision surgery, and to plan the procedure.

REFERENCES

1. Kingsnorth A. Treating inguinal hernias. *BMJ.* 2004;328:59 60.
2. Rutkow IM. Demographic and socioeconomic aspects of hernia repair in the United States in 2003. *Surg Clin North Am.* 2003;83:1045 1051.
3. Burger JW, Luijendijk RW, Hop WC, et al. Long-term follow-up of a randomized controlled trial of suture versus mesh repair of incisional hernia. *Ann Surg.* 2004;240:578 583.
4. Penttinen R, Groenroos JM. Mesh repair of common abdominal hernias: a review on experimental and clinical studies. *Hernia.* 2008;12:337 344.
5. Eriksen JR, Goegenur I, Rosenberg J. Choice of mesh for laparoscopic ventral hernia repair. *Hernia.* 2007;11:481 492.
6. Klinge U, Klosterhalfen B, Birkenhauer V, et al. Impact of polymer pore size on the interface scar formation in a rat model. *J Surg Res.* 2002;103:208 214.

7. Leber GE, Garb JL, Alexander AI, et al. Long-term complications associated with prosthetic repair of incisional hernias. *Arch Surg*. 1998;133: 378 382.

8. Aasvang EK, Bay-Nielsen M, Kehlet H. Pain and functional impairment 6 years after inguinal herniorrhaphy. *Hernia*. 2006;10:316 321.

9. Massaron S, Bona S, Fumagalli U, et al. Long-term sequelae after 1311 primary inguinal hernia repairs. *Hernia*. 2007;12:57 63.

10. Eklund A, Montgomery A, Bergkvist L, et al. Chronic pain 5 years after randomized comparison of laparoscopic and Lichtenstein inguinal hernia repair. *Br J Surg*. 2010;97:600 608.

11. Hamouda A, Kennedy J, Grant N, et al. Mesh erosion into the urinary bladder following laparoscopic inguinal hernia repair; is this the tip of the iceberg? *Hernia*. 2010;14:317 319.

12. Fischer T, Ladurner R, Gangkofer A, et al. Functional cine MRI of the abdomen for the assessment of implanted synthetic mesh in patients after incisional hernia repair: initial results. *Eur Radiol*. 2007;17:3123 3129.

13. Lienemann A, Sprenger D, Steitz HO, et al. Detection and mapping of intraabdominal adhesions by using functional cine MR imaging: preliminary results. *Radiology*. 2000;217:421 425.

14. Zinther NB, Zeuten A, Marinovskij E, et al. Functional cine MRI and transabdominal ultrasonography for the assessment of adhesions to implanted synthetic mesh 5 7 years after laparoscopic ventral hernia repair. *Hernia*. 2010;14:499 504.

15. Kirchhoff S, Ladurner R, Kirchhoff C, et al. Detection of recurrent hernia and intraabdominal adhesions following incisional hernia repair: a functional cine MRI-study. *Abdom Imaging*. 2010;35:224 231.

16. Widmaier S, Jung WI, Pfeffer K, et al. MRI and determination of T1 and T2 of solid polymers using a 1.5 T whole-body imager. *Magn Reson Imaging*. 1993;11:733 737.

17. Springer F, Martirosian P, Schwenzer N, et al. Three-dimensional ultrashort echo time imaging of solid polymers on a 3-Tesla whole-body MRI scanner. *Invest Radiol*. 2008;43:802 808.

18. Kraemer NA, Donker HC, Otto J, et al. A concept for magnetic resonance visualisation of surgical textile implants. *Invest Radiol*. 2010;45:477 483.

19. Donker HC, Kraemer NA, Otto J, et al. Mapping of proton relaxation near superparamagnetic iron oxide particle-loaded polymer threads for magnetic susceptibility difference quantification. *Invest Radiol*. 2012;47:359 367.

20. Slabu I, Guentheradt G, Schmitz-Rode T, et al. Investigation of superparamagnetic iron oxide nanoparticles for MR-visualization of surgical implants. *Curr Pharm Biotechnol*. 2012;13:545 551.

21. Kuehnert N, Kraemer NA, Otto J, et al. In vivo MRI visualization of mesh shrinkage using surgical implants loaded with superparamagnetic iron oxides. *Surg Endosc*. 2012;26:1468 1475.

22. Kraemer NA, Donker CW, Kuehnert N, et al. In vivo visualization of polymer-based mesh implants using conventional magnetic resonance imaging and positive-contrast susceptibility imaging. *Invest Radiol*. 2013;48:200 205.

23. Arregui ME, Davis CJ, Yucel O, et al. Laparoscopic mesh repair of inguinal hernia using preperitoneal approach: a preliminary report. *Surg Laparosc Endosc*. 1992;2:53 58.

24. Lichtenstein IL, Shulman AG, Amid PK, et al. The tension-free hernioplasty. *Am J Surg*. 1989;157:188 193.

25. Amid PK, Shulam AG, Lichtenstein IL. A critical scrutiny of the open tension-free hernioplasty. *Am J Surg*. 1993;165:369 371.